https://dx.doi.org/10.1016/j.watres.2020.116106

Contrasting Abiotic As(III) Immobilization by Undissolved and Dissolved Fractions of Biochar in Ca^{2+}-Rich Groundwater under Anoxic Conditions

Delai Zhong[a, b], Zezhou Zhao[a], Yi Jiang[b], Xiao Yang[b, c], Linling Wang[a, *], Jing Chen[a], Chung-Yu Guan[b, d], Yanrong Zhang[a], Daniel C.W. Tsang[b], John C. Crittenden[e]

[a] *School of Environmental Science and Engineering, Huazhong University of Science and Technology, Wuhan, 430074, China*

[b] *Department of Civil and Environmental Engineering, The Hong Kong Polytechnic University, Hung Hom, Kowloon, Hong Kong, China*

[c] *Korea Biochar Research Center, Division of Environmental Science and Ecological Engineering, Korea University, Korea*

[d] *Graduate Institute of Environmental Engineering, National Taiwan University, Taipei 106, Taiwan*

[e] *Brook Byers Institute of Sustainable Systems and School of Civil and Environmental Engineering, Georgia Institute of Technology, Atlanta, Georgia 30332, United States*

* Corresponding author. E-mail address: wanglinling@hust.edu.cn (L. Wang).

Abstract

Engineered black carbon (biochar) can be introduced into groundwater through its extensive engineered applications (e.g., *in-situ* remediation of groundwater/soils), which can participate in geochemical processes that may alter the fate of trace contaminants such as arsenic (As(III)). Here we examined the impacts of the undissolved and dissolved fractions of reduced biochar (hereafter denoted as rUBC and rDBC, respectively) on the As(III) immobilization in the absence/presence of Ca^{2+} (50 mM) at pH 11.5 under anoxic conditions. While neither rUBC nor rDBC alone was capable of immobilizing As(III), the apparent As(III) immobilization by rUBC and rDBC synergistically occurred in the presence of Ca^{2+}, with an efficiency of 73.1% and 89.6% within 24 h, respectively. In the rUBC/Ca^{2+}/As(III) system, rUBC enabled full oxidation of As(III) to As(V) by its residual redox-active moieties such as quinoid C=O and persistent free radicals, thereby facilitating precipitation of the newly generated As(V) with Ca^{2+} adsorbed onto the rUBC's surface. In contrast, rDBC induced *in-situ* local enrichment of Ca^{2+} in the nascent rDBC-derived flocs with predominant non-oxidative and slight oxidative precipitation of As(III) via ternary rDBC-Ca-As complexation. This ternary complex was created by Ca^{2+}-bridging interactions between As species and oxygen-containing functional groups of rDBC, as evidenced by the FTIR results and the Ca^{2+}-impeded As(III) oxidation. The generation of the flocs physically trapped a small amount of As species particularly As(III). Both the increases in Ca^{2+} concentration (0–100 mM) and solution pH (10.0–12.5) enhanced the apparent As(III) immobilization. This study provides new insights into the environmental

impacts of two reduced biochar fractions released into typical Ca^{2+}-rich aquifers on the fate and transport of As species.

Keywords: Arsenic contamination; Synergistic immobilization; Abiotic mechanisms; Undissolved and dissolved biochar; Calcium-rich aquifer

1. Introduction

High-arsenic (As) contamination in groundwater is a recognized global environmental problem (Smedley and Kinniburgh, 2002). Ingesting high-As groundwater can pose severe threats to public health, such as skin lesions and even cancer (Karim, 2000). A previous study suggested that approximately 19.6 million residents in China might be exposed to unsafe As levels, i.e., above the World Health Organization (WHO) guideline of 10 μg/L (Rodríguez-Lado et al., 2013). It is widely recognized that As concentration in groundwater is intimately governed by its interactions with major co-existing minerals (e.g., iron (Fe) oxyhydroxides) via geochemical processes including precipitation/dissolution and adsorption/desorption. Therefore, it is paramount to identify and understand the geochemical processes that control the fate of As in aquifers. To date, numerous studies have well revealed that elevated As concentration in groundwater is predominantly triggered by both reductive dissolution of As-rich Fe oxyhydroxides and alkaline pH-induced desorption (Michael, 2013). Such phenomenon commonly occurs in As-contaminated aquifers, with abundant concomitant Fe oxyhydroxides, of South and Southeast Asia (Fendorf et al., 2010; Michael, 2013;

Podgorski et al., 2017).

Nevertheless, anomalous As concentration is frequently observed in some calcium (Ca)-rich aquifers (e.g., calcareous aquifers) (Winkel et al., 2013), particularly in highly alkaline conditions (pH value up to 10~13) as a result of natural processes and/or anthropogenic activities (Barnes et al., 1982; Mariner et al., 1996; Sadergaski et al., 2019). The fate and transport of As in the aquifers is more profoundly affected by co-existing Ca if the Ca is sufficiently high concentration (even up to tens of mmol/L) in cases where: (1) the average Fe concentration is low (below 0.002 mmol/L), or (2) its minerals have lost adsorption efficacy. (Guo et al., 2014; Martínez-Villegas et al., 2013; Winkel et al., 2013). For example, Zhang and Yang (2013) proposed that As in underground sediment of the calcareous regions was correlated with Ca in both water bodies and sediments. It was also claimed that As in the calcareous regions was detected to be highly enriched in natural Ca-containing minerals up to two orders of magnitude over the normal crustal As abundances (Costagliola et al., 2013). Besides, Qian et al. (2015) demonstrated that the presence of Ca^{2+} could significantly promote As(III) oxidation/precipitation. In addition to Ca^{2+}, natural organic matter (NOM) is ubiquitous in natural/engineered waters and plays a critical role in the (bio)geochemical cycling of trace As (Lawson et al., 2013; Mak et al., 2009; Reza et al., 2010). For instance, the presence of NOM can hinder the increased role of Ca^{2+} in As removal from NOM-rich groundwater by competing with As for binding sites (Mak et al., 2009). Moreover, the co-presence of NOM and Ca^{2+} has been reported to trigger the aggregation (Liu et al., 2008), which may thereby facilitate As removal. In contrast to many investigations on

NOM, to the best of our knowledge, we are the first to report the impacts of engineered constituents (e.g., engineered black carbon) on the fate of As in the anoxic Ca^{2+}-rich groundwater (e.g., calcareous groundwater).

Biochar, as a representative of engineered black carbon, has attracted increasing interest in environmental and agricultural applications due to its favorable physical, chemical, and biocompatibility properties in recent years (Cao et al., 2011; Wei et al., 2018; Yang et al., 2019; Yao et al., 2013). The extensive engineered applications of biochar, including *in-situ* remediation of groundwater/soils (Bortone et al., 2013; Mackenzie et al., 2012; Wei et al., 2018) and managed aquifer recharge (which carries biochar) (Rauch-Williams et al., 2010), have resulted in its introduction into subsurface environments. This has been shown by the presence of (in the range of ca. 1–40%) biochar-derived organic carbon that has been detected in soils and sediments (Jin et al., 2017; Lian and Xing, 2017; Zimmerman, 2010). The introduced biochar can be found as both undissolved and dissolved fractions (hereafter denoted as UBC and DBC, respectively) in wet and anoxic environments, especially for shallow groundwater. Analogous to NOM (Roden et al., 2010; Scott et al., 1998), they can be chemically or microbially reduced in the environments to a certain extent. Furthermore, they can potentially participate in (bio)geochemical processes that alter the fate of the co-existing contaminants such as As (Beiyuan et al., 2017; Niazi et al., 2018a; Vithanage et al., 2017; Yang et al., 2018b). It has been well recognized that both UBC and DBC have significant differences in structural configuration and chemical composition (e.g., element contents and types), thus endowing their contrasting physicochemical

properties (e.g., surface charge, complexation, and redox properties) (Qu et al., 2016; Yang et al., 2018a). Therefore, it can be rationally hypothesized that the two reduced UBC and DBC play different, even contrasting roles in the fate of As in groundwater.

UBC constitutes active components in bulk biochar and often plays a primary role in the immobilization and redox transformation of As via various interaction mechanisms (Niazi et al., 2018a; Qiao et al., 2018; Vithanage et al., 2017; Zhong et al., 2019). For example, both perilla-leaf- and Japanese oak-wood-derived biochar particles immobilized As species with capacities of 3.85–11.01 mg/g via both surface complexation and precipitation (Niazi et al., 2018a; Niazi et al., 2018b). Further As(III) oxidation was found on the two UBCs. In our recent study, rice-husk-derived biochar particles negligibly immobilized As species in the pH range of 3.0–9.5, while As(III) oxidation occurred (Zhong et al., 2019). These studies, however, failed to examine the impacts of other naturally existing constituents such as Ca^{2+} on these processes in the co-presence of UBC, especially under anoxic conditions. On one hand, UBC can oxidize As(III) to As(V) due to the presence of redox-active moieties (RAMs) in spite of anoxic conditions (Zhong et al., 2019). On the other hand, Ca^{2+} can be readily adsorbed onto negatively charged UBC, which may improve redox interactions between UBC and the negatively charged As anions by neutralizing UBC's surface negative charge (Marshall et al., 2017). Taken together, the presence of Ca^{2+} play a significant role in enhancing As(III) oxidation and subsequent immobilization by UBC in groundwater. In contrast to numerous studies on UBC, the effect of DBC on the (im)mobilization and redox transformation of As is often underestimated and poorly

131 understood (Dong et al., 2014; Vithanage et al., 2017), presumably the presence/impact
132 of DBC that has been neglected by many researchers. DBC possesses more oxygen-
133 containing functional groups (OFGs), lower aromaticity, and smaller fused aromatic
134 clusters than UBC (Qu et al., 2016; Yang et al., 2018a). The abundant OFGs of DBC
135 may compete with As(III) for binding sites and complex As(III) to generate dissolved
136 As complex, consequently promoting As mobility. However, Ca^{2+} can elevate the ionic
137 strength of solution and decrease the negative charge of DBC, both of which can trigger
138 the aggregation and precipitation of DBC (Xu et al., 2017). As a result, Ca^{2+} is
139 anticipated to be highly enriched in the aggregates and may subsequently stimulate
140 chemical precipitation with As. Despite the redox inertness of Ca^{2+}, it may protect
141 semiquinone free radicals within DBC by Ca^{2+}-bridging interactions and -inducing
142 intramolecular aggregation to reduce As(III) oxidation, similar to the effect of Ca^{2+} on
143 the properties of NOM (Palmer and von Wandruszka, 2001; Yates and von Wandruszka,
144 1999). Thus, the presence of Ca^{2+} would complicate the oxidation and immobilization
145 of As(III). Despite the significant understanding of the fate of As in groundwater, to
146 date, we still lack knowledge regarding the effects of the reduced UBC and DBC on the
147 oxidation and immobilization of As(III) in anoxic Ca^{2+}-rich groundwater.

148 Herein we prepared the undissolved and dissolved fractions of reduced rice-husk-
149 derived biochar to explore their respective effects on the oxidation and immobilization
150 of As(III) in simulated alkaline Ca^{2+}-rich groundwater. We integrated wet chemistry
151 experiments and multiple spectroscopic characterizations to elucidate the mechanisms
152 of As(III) immobilization in the co-presence of biochar and Ca^{2+}. In addition, the effect

of water chemistry, including Ca^{2+} concentration (0–100 mM) and solution pH (10.0–12.5), was examined. The knowledge of this study can advance our understanding of the environmental effects and implications of rUBC and rDBC released into alkaline Ca^{2+}-rich groundwater on the fate of As(III).

2. Materials and methods

2.1. Chemicals

All the chemicals used in this study are described in Text S1 of Supporting Information (SI).

2.2. Preparation of rUBC and rDBC and characterization

Biochar was typically produced by oxygen-limited pyrolysis of rice husk, and more details were provided in our previous study (Zhong et al., 2019). In brief, each 30 g of rice husk was placed in a silicon carbide vessel with cap and subsequently pyrolyzed in a muffle furnace under oxygen-limited conditions at 400 ℃ for 1 h. Afterwards, the biochar sample was cooled to room temperature for collection. To simulate the reduced state of biochar released into anoxic groundwater, we performed the reduction experiment using the biochar suspension and a typically chemical reduction method in the dark according to a previous report (Roden et al., 2010). After the reduction, the biochar suspension was filtered using a 0.22 μm nylon membrane which is similar to a previous study (Yang et al., 2018a). The reduced rUBC and rDBC are the retentate and permeate, respectively. More details involving the reduction and

fractionation procedures are presented in Text S2 of SI. The resulting reduced biochar fractions were hereby referred to as rUBC and rDBC, respectively, and stored at 4 °C in the dark before use.

The characterizations including the morphologies, surface chemical properties, crystalline structures, and elemental compositions are provided in detail in Text S3 of SI.

2.4. As(III) immobilization experiments

Unless otherwise specified, all batch experiments were conducted in a 250-mL magnetically stirred reactor filled and equilibrated with a 100% N_2 (under a standard atmosphere pressure) at room temperature in the dark. Before the As(III) immobilization experiments, all solutions (e.g., rDBC solution) were sparged with ultrapure nitrogen for at least 2 h, and all materials (e.g., rUBC and $CaCl_2 \cdot 2H_2O$) were deoxygenated in a vacuum for at least 2 h. For the rUBC systems, 0.2 g of rUBC was added into 100 mL of 100 μM As(III) solution to create 2 g/L rUBC suspension, then adjusted to pH 11.5±0.1 with 0.01 and 0.1 M NaOH solution. Afterwards, the concurrent introductions of 0.735 g of $CaCl_2 \cdot 2H_2O$ powder (equal to 50 mM Ca^{2+} in the resulting solution) and a desired amount of the NaOH solution into the suspension were performed to initiate the As(III) immobilization reaction for 24 h (NaOH solution was added again because the introduction of $CaCl_2 \cdot 2H_2O$ powder would result in a serious decrease in the suspension pH). Desired reaction suspensions were filtrated with 0.22 μm nylon membrane. The dissolved As species was the permeate. A 1 M HCl

digestion was used to measure the total As species (As(tot)) in the unfiltered samples. The immobilization fraction of each As species was calculated by subtracting the concentration of each As species in the aqueous-phase from that of the corresponding As(tot) species in the unfiltered samples. For the rDBC As(III) immobilization tests, a 156±5 mg rDBC as carbon/L (mg C/L) stock solution was used and the tests were conducted in the same manner as those used for the scenarios described above. Meanwhile, we also performed control experiments in the absence of either biochar (i.e., rUBC and rDBC) or Ca^{2+} under the same experimental conditions. All the experiments were performed in triplicate. In addition, the effects of Ca^{2+} concentration (0–100 mM) and solution pH (10.0–12.5) on the As(III) immobilization were investigated.

2.5. Analytical methods

The As(III) and As(V) concentrations were measured by using a high performance liquid chromatography (HPLC, LC-100^{PLUS}, Shanghai Wufeng Scientific Instrument Co., Ltd.) coupled to a hydride generation-atomic fluorescence spectrometer (HG-AFS, SA7800, Beijing Bohui Innovation Optoelectronic Technology Co., Ltd.). More details on the analysis of As species were described in our recent document (Zhong et al., 2019). There were no organic As species; consequently, we assumed that As(tot) was equal to the sum of As(III) and As(V) for both rUBC and rDBC.

3. Results and discussion

3.1. Apparent As(III) immobilization associated with the presence of rUBC and rDBC

Fig. 1a below shows that, in the Ca^{2+}/As(III) system, no observable immobilization of As(III) by 50 mM of Ca^{2+} occurred at pH 11.5 under anoxic conditions, which was consistent with no formation of Ca-As(III) precipitates as predicted by MINEQL+4.6 model that is based on equilibrium chemical precipitation reactions (Fig. 1b). This observation demonstrates that As(III) remained stable in the Ca^{2+}-rich solution at pH 11.5, that is, 50 mM of Ca^{2+} was not capable of immobilizing As(III). Upon the introduction of rUBC into the Ca^{2+}/As(III) system, the apparent As(III) immobilization (i.e., the sum of As(III) and As(V) immobilization) increased gradually from 0 to 73.1 μM within 24 h (Fig. 1a). In contrast, our control experiment in the absence of Ca^{2+} revealed that rUBC could not immobilize As(III), which was ascribed to the following facts: (1) the strong electrostatic repulsion between As anions (predominant forms of $HAsO_3^{2-}$, H_2AsO^{3-}, $HAsO_4^{-}$, and AsO_4^{3-}, Fig. S1) and the negatively charged surface of rUBC (–38.1 mV, Fig. S2) (He et al., 2018; Van Vinh et al., 2015); (2) the strong competitive adsorption between As anions and OH^- (Goh and Lim, 2004); (3) the limited BET-surface area of rUBC (37.3 m^2/g). The results indicate that both rUBC and Ca^{2+} synergistically enabled the apparent As(III) immobilization. Unlike the immobilization in the rUBC/Ca^{2+}/As(III) system, the apparent As(III) immobilization sharply jumped from 0 to 65.1 μM within 0.5 h, and gradually increased to 89.6 μM afterward in the rDBC/Ca^{2+}/As(III) system (Fig. 1a). The details are further discussed later in Section 3.2. No apparent As(III) immobilization by rDBC occurred in the Ca^{2+}-free solution and this is probably due to the formation of water-soluble mixture and/or complex (which can pass through 0.22 μm nylon membrane). Although both rUBC and

241 rDBC participated in the apparent As(III) immobilization in the presence of Ca^{2+}, they
242 might play different roles in the immobilization processes, as highlighted by the
243 significant discrepancies in the aforementioned immobilization behavior (Fig. 1a).
244

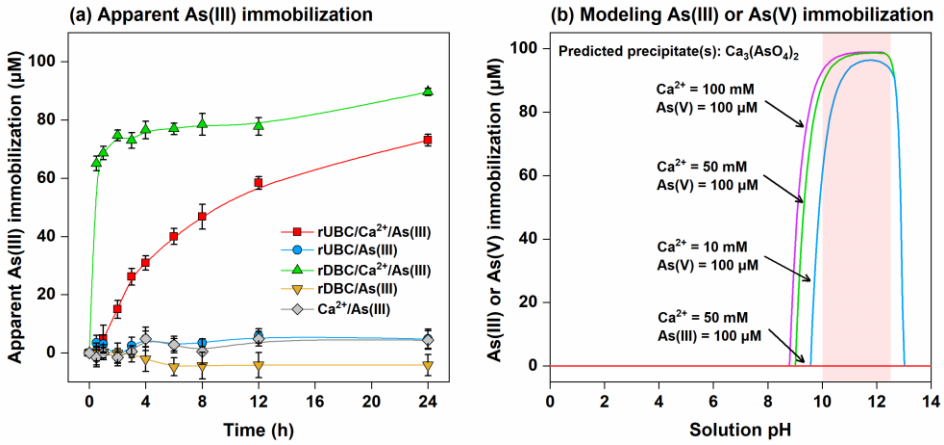

245

246 **Fig. 1.** (a) Apparent As(III) immobilization as a function of reaction time in different
247 systems; (b) modeling As(III) or As(V) immobilization as a function of solution pH in
248 different biochar-free systems using MINEQL+4.6 based on the equilibrium
249 precipitation reactions. For (a): the initial concentrations of rUBC, rDBC, As(III), and
250 Ca^{2+} were 2 g/L, 156±5 mg C/L, 100 μM, and 50 mM, respectively; the system pH was
251 maintained at 11.5±0.1; the reaction time was 24 h; for (b): the initial concentrations of
252 As(III), As(V), and Ca^{2+} were 100 μM, 100 μM, and 10–100 mM, respectively.
253

254 *3.2. rUBC-induced oxidative precipitation of As(III) with Ca^{2+}*

255 Biochar particles, as predominant reactive sinks, have been reported to participate
256 in redox reactions with some pollutants such as As and Cr (Niazi et al., 2018a; Wongrod
257 et al., 2019; Zhong et al., 2019; Zhong et al., 2018). In combination with our
258 experimental observations (Fig. 1a), we hypothesize that rUBC might interact with

As(III) (e.g., redox reaction) and increase the apparent As(III) immobilization with Ca^{2+}, It is important to note that neither rUBC nor Ca^{2+} alone is capable of immobilizing As(III). To verify this hypothesis, we first explored the potential interactions of rUBC alone with As(III) in the absence of Ca^{2+}. As(III) in the solution was found to be completely oxidized by rUBC within 8 h; and, the newly generated As(V) concentration in the solution increased significantly from 0 to 100 μM (Fig. 2a). In contrast, our control experiment without rUBC revealed that As(III) could not be oxidized to As(V) for the same conditions (data not shown). These findings suggest that rUBC could fully oxidize As(III) to As(V) at pH 11.5, as further supported by recent studies (Niazi et al., 2018a; Niazi et al., 2018b; Zhong et al., 2019). This As(III) oxidation could be a result of the presence of residual redox-active moieties (RAMs), particularly quinoid C=O (1705 cm^{-1}) and persistent free radicals (PFRs) on rUBC (Fig. S3) (Dong et al., 2014; Wan et al., 2020; Zhong et al., 2019).

As(V) has been well documented to have a higher binding affinity for Ca^{2+} than As(III) (Tokunaga, 1999). Consequently, the oxidation of As(III) by rUBC to generate As(V) would benefit the formation of Ca-As(V) precipitates and apparent As(III) immobilization at pH 11.5 (Wang et al., 2019), when Ca^{2+} was introduced into the rUBC/As(III) system. This was further evidenced by the model prediction which showed that As(V) completely precipitates as $Ca_3(AsO_4)_2$ at pH 11.5 (i.e., the concentrations of Ca^{2+} and As(V) were 50 mM and 100 μM, respectively) (Fig. 1b). It is worth noting that the model prediction (100.0%) is far higher than that (73.1%) in the rUBC/Ca^{2+}/As(III) system, presumably due to the presence of rUBC.

While this proposed hypothesis is plausible, solid evidences favoring it are further invoked. We therefore scrutinized the oxidation and solid-liquid partitioning of As(III) in the rUBC/Ca^{2+}/As(III) system. In the aqueous phase, we observed the accelerated and complete removal of As(III) (more precisely, the accelerated As(III) oxidation in the aqueous phase, see below), as compared with that in the absence of Ca^{2+} (Fig. 2b). Ca^{2+} is a redox-inert component and not capable of oxidizing As(III), as further confirmed by no production of As(V) in the Ca^{2+}/As(III) system (Fig. S4). Hence, we attribute the positive effect of Ca^{2+} to the enhanced interactions between As(III) anions and RAMs (e.g., quinoid C=O and PFRs on rUBC) by neutralizing the negative charge on surface of rUBC with the Ca^{2+} adsorption/precipitation (Figs. S2 and S5). Furthermore, the newly generated As(V) concentration in the solution increased significantly from 0 to 71.0 μM within 3 h, but decreased to 27.0 μM afterward. This trend implies that As(V) was first generated from As(III) oxidation by rUBC and was gradually immobilized thereafter. This was corroborated by the observation that the As(V) concentration in the solid phase significantly increased to 72.2 μM within 24 h (Fig. 2b). However, no detectable As(III) was found in the solid phase (Fig. 2b), which is approximately due to the complete As(III) oxidation and/or its considerably low affinity for both Ca^{2+} and rUBC at pH 11.5. Based on all the experimental observations and analyses, we suggest that As(III) was oxidized to As(V) by rUBC, and then the newly generated As(V) in the solution primarily precipitates with the adsorbed/precipitated Ca^{2+} onto the surface of rUBC.

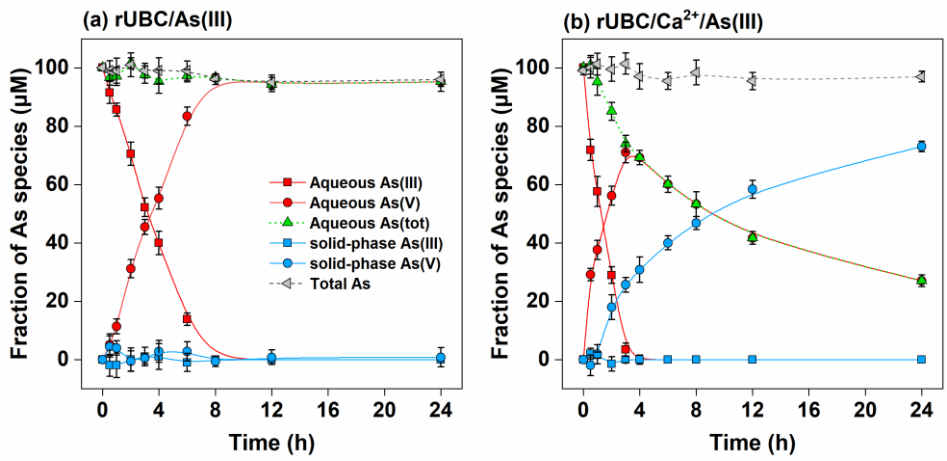

Fig. 2. Oxidation and partitioning of As(III) in the (a) rUBC/As(III) and (b) rUBC/Ca^{2+}/As(III) systems. The initial concentrations of rUBC, As(III), and Ca^{2+} were 2 g/L, 100 μM, and 50 mM, respectively; the system pH was maintained at 11.5±0.1; the reaction time was 24 h.

We further performed several selected spectroscopic characterizations including SEM-EDS, FTIR, XPS, and XRD to prove that the proposed As(III) oxidative immobilization occurs. Using SEM-EDS characterization, we first visualized the morphologies of rUBC samples collected at the selected reaction stages (hereafter denoted as rUBC-0.5, rUBC-8, and rUBC-24, respectively). As shown in Fig. 3a, rUBC (as the control sample) had a smooth surface with no deposition of precipitates on its surface. The corresponding EDS elemental mappings analysis revealed that major elements were C and O, and no Ca and As (only elements of interest) were on the pristine rUBC (Fig. 3b–3e). A small amount of the microparticles deposited on the surface of rUBC-0.5 was observed when the reaction time was increased to 0.5 h, though its surface seemed smooth (Fig. 3f). The abundant element Ca was uniformly distributed in rUBC-0.5, whereas negligible As was detected probably due to a

considerably low concentration of As immobilized in rUBC-0.5 (Fig. 3i and 3j). Both the surfaces of rUBC-8 and rUBC-24 became far rougher; meanwhile, an increasing number of microparticles with larger size were visualized in rUBC-8 and rUBC-24 when the reaction time was further prolonged to 8 or 24 h (Fig. 3k and 3p). Both the elements Ca and As were further enriched in rUBC-8 and rUBC-24 (Fig. 3n, 3o, 3s, and 3t), and the distribution of As was closely collocated with that of Ca. These results further confirm that Ca^{2+} was adsorbed onto the surface of rUBC and followed by precipitation with As on its surface.

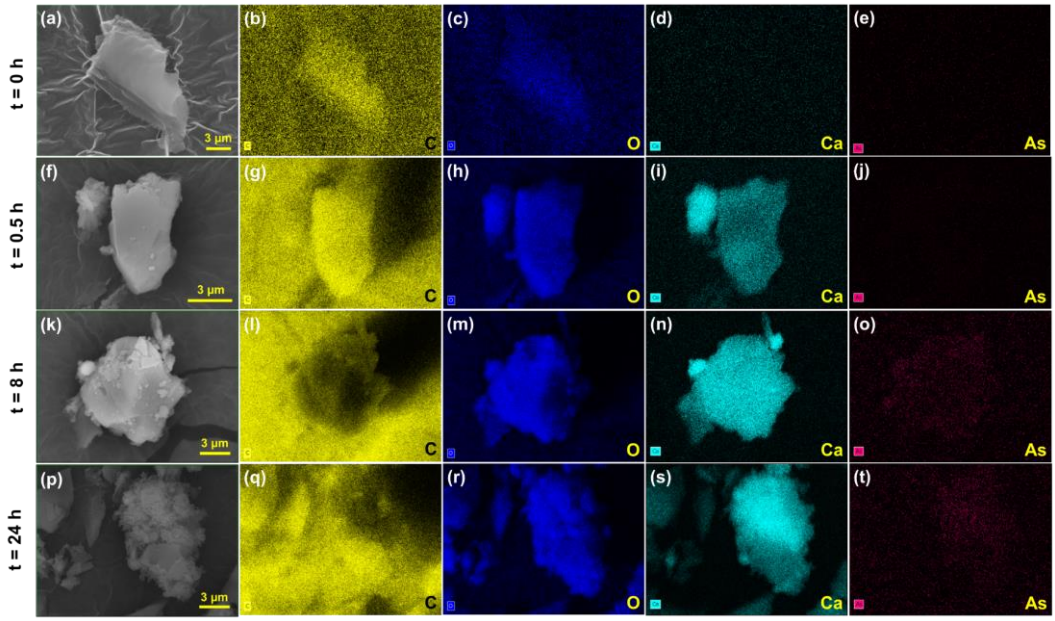

Fig. 3. SEM images (a, f, k, and p) and the corresponding EDS elemental mappings of the freeze-dried samples collected from the rUBC/Ca^{2+}/As(III) system during the As(III) immobilization: element C (b, g, l, and q), O (c, h, m, and r), Ca (d, i, n, and s), As (e, j, o, and t).

FTIR was employed to examine changes in chemical properties of these samples

during the As(III) immobilization. Fig. 4a demonstrates no detectable changes in peaks at 1613 cm^{-1} (aromatic C=C), 1384 cm^{-1} (aliphatic $–CH_3$), 1100 cm^{-1} (aliphatic C–O–C, C–OH, and C–O), and 800 cm^{-1} (aromatic C–H). The FTIR results suggest that these functional groups were not involved in the As(III) immobilization. However, we found a significant decrease in relative peak intensity of quinoid C=O at 1705 cm^{-1}, suggesting that quinoid C=O participated in the As(III) oxidation (Zhong et al., 2019). This was supported by the similar observation that benzoquinone could oxidize As(III) to As(V) under slightly alkaline conditions (Qin et al., 2016). In comparison with rUBC, three new peaks at 700–1500 cm^{-1} gradually appeared, and their relative peak intensities presented the elevated trends when the reaction time was extended from 0.5 to 24 h. Specifically, a new characteristic peak at 875 cm^{-1} was attributed to the stretching vibration of Ca–O–As^{V} and Ca–O, indicating the formation of Ca-As(V) precipitates (Zhang et al., 2015). Meanwhile, a small peak was detected at 712 cm^{-1} and was assigned to the As^{V}–O(H) stretching vibration of Ca-As(V) precipitates (Zhang et al., 2015). In addition, another characteristic peak was detected at 1482 cm^{-1}, corresponding to the C–O–C stretching vibration of $CaCO_3$, which was presumably due to interaction of atmospheric CO_2 with Ca^{2+} under alkaline conditions (Hu et al., 2014).

From the As $3d_{5/2}$ XPS spectra in Fig. 4b, it was observed that only a peak appeared at ~44.2 eV assigned to As(V), and its relative peak intensity exhibited an elevating trend with reaction time, indicating the increasing generation of Ca-As(V) precipitates on the surfaces of these samples. Further XRD examination revealed that the Ca-As(V) precipitates were attributed to amorphous mineral, because they did not have

characteristic XRD peaks of Ca-As(V) components (Fig. 4c). Overall, all spectroscopic characterization observations and analyses were in good agreement with the aforementioned wet chemistry results, supporting the proposed oxidative As(III) immobilization by rUBC via the generation of Ca-As(V) precipitates on the surface of rUBC.

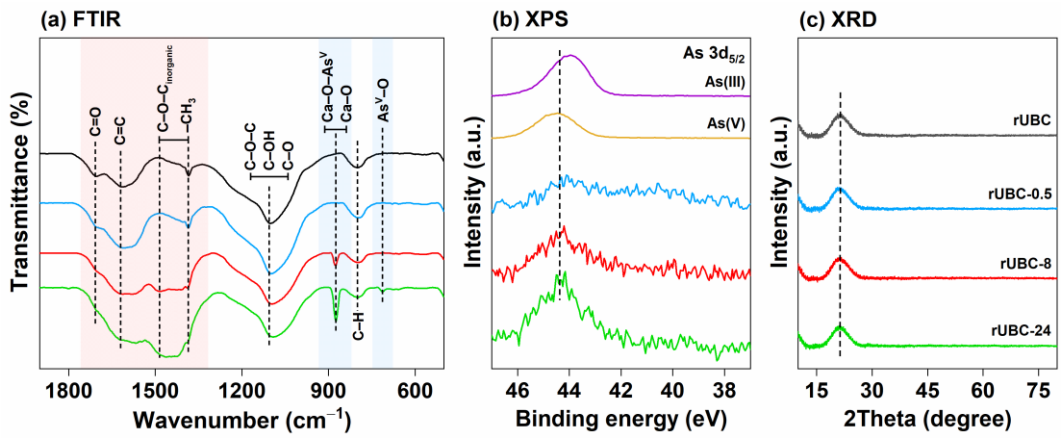

Fig. 4. (a) FTIR spectra, (b) As $3d_{5/2}$ XPS spectra, and (c) XRD patterns of the selected rUBC samples.

3.3. In-situ creation of highly enriched Ca^{2+} flocs with rDBC drives multiple As(III) immobilization

Similar to UBC, DBC has been reported to oxidize As(III) under alkaline conditions (Dong et al., 2014). This motivates us to examine the oxidation of As(III) and partitioning of As(III)/produced As(V) by rDBC in the absence of Ca^{2+}. As shown in Fig. 5a, all of the As species was present in the aqueous phase. Furthermore, only a small amount (19.3 μM) of As(III) in this phase was oxidized to As(V) by rDBC due to the presence of quinoid C=O and PFRs (Fig. S3). Only As(V) could be fully

immobilized by chemical precipitation with 50 mM of Ca^{2+} in the rDBC-free solution at pH 11.5 (Fig. S6). These results suggest that, in the rDBC/Ca^{2+}/As(III) system, the apparent As(III) immobilization might not be predominantly governed by the aforementioned oxidative As(III) precipitation with Ca^{2+}, as implied by our previous observations (Fig. 1a). As shown in Fig. 5b, after the introduction of Ca^{2+} into the rDBC/As(III) system, the oxidation and partitioning of As(III) became different from those in the rUBC/Ca^{2+}/As(III) system. In particular, the As(III) concentration in the solution dropped dramatically down from 100 to 26.4 μM within 0.5 h, but the As(V) concentration increased slightly from 0 to 8.6 μM. Afterwards, they maintained a slightly decreasing trend. Meanwhile, in the solid phase the As (III) concentration increased significantly from 0 to 60.6 μM within 0.5 h, whereas the As(V) concentration rose slightly to 4.4 μM. Unlike the positive effect of Ca^{2+} on the As(III) oxidation by rUBC, we found that the presence of Ca^{2+} could impede the oxidation of As(III) to As(V) by rDBC (Fig. 5). Recently, a similar phenomenon was observed for the negative effect of Ca^{2+} on the ferrous oxidation by NOM (Jiang et al., 2017). This impediment might be because the redox-inert Ca^{2+} adsorbed/precipitated on the surface inhibited electron transfers between As(III) and rDBC and this reduced As(III) oxidation. Overall, these results clarify that most of As(III) was non-oxidatively immobilized by both rDBC and Ca^{2+}. Also, these findings highlight that the As(III) oxidative immobilization was not a major pathway in the rDBC/Ca^{2+}/As(III) system and other possible mechanisms were likely to be involved.

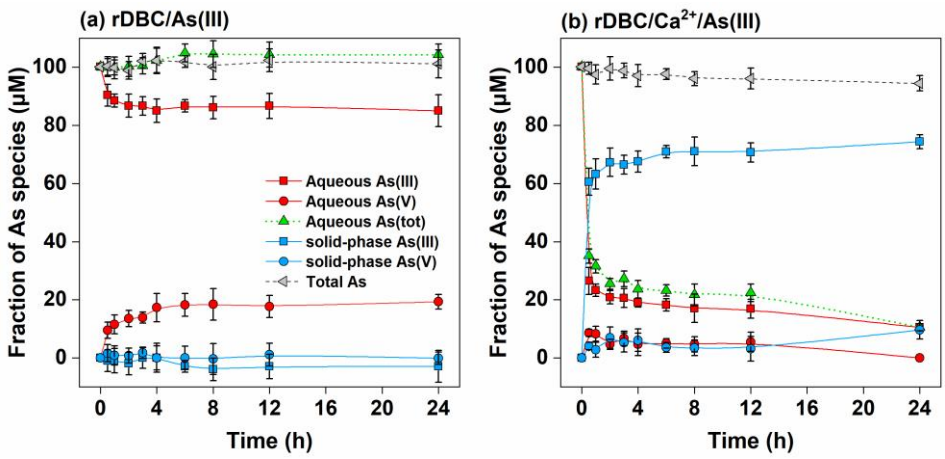

397

398 **Fig. 5.** Oxidation and partitioning of As(III) in the (a) rDBC/As(III) and (b)
399 rDBC/Ca^{2+}/As(III) systems. The initial concentrations of rDBC, As(III), and Ca^{2+} were
400 156±5 mg C/L, 100 μM, and 50 mM, respectively; the system pH was maintained at
401 11.5±0.1; the reaction time was 24 h.

402

403 Unlike the absence of visible precipitates in our control systems (i.e., the
404 Ca^{2+}/As(III) and the DBC/As(III) systems), we noticed an extraordinary phenomenon
405 that plenty of light brown flocs *in-situ* were generated upon the introduction of Ca^{2+}
406 into the rDBC/As(III) system (Fig. S7). A similar observation was found in the study of
407 Ca^{2+} on the aggregation behavior of dissolved biochar at circumneutral pH (Xu et al.,
408 2017). This generation resulted from the significant aggregation of intramolecular
409 within rDBC via two successive interactions: (1) Ca^{2+} neutralized some of the negative
410 surface charge of rDBC to weaken electrostatic repulsion between intramolecular
411 within rDBC (Figs. S2 and S5) (Xu et al., 2017); (2) Ca^{2+} subsequently bridged rDBC
412 to promote the intimate contact each other (Yang et al., 2018a). The resulting flocs
413 enabled the collective precipitation of As, Ca^{2+}, and rDBC, as indicated by SEM-EDS
414 analysis below (Fig. 6). There are three possible pathways accounting for the apparent

As(III) immobilization in the rDBC/Ca^{2+}/As(III) system: (1) complexation of As with rDBC-derived oxygen-containing functional groups (OFGs) in the flocs; (2) physical enmeshment of As by the nascent rDBC-Ca flocs; (3) chemical precipitation of As with highly enriched Ca^{2+} in the flocs. Since OFGs generally possess a lower affinity for As than Ca^{2+} particularly under highly alkaline conditions, we can rule out the complexation pathway that causes the apparent As(III) immobilization. Subsequently, we checked physical enmeshment by delicately creating the rDBC-Ca flocs *in-situ* for the As(III) immobilization (i.e., both rDBC and Ca^{2+} were first allowed to generate the flocs for 0.5 h, then the resulting flocs was employed to immobilize As(III) for another 24 h and were denoted as (rDBC/Ca^{2+})/As(III)). As shown in Fig. S8, the physical enmeshment was estimated to approximately contribute to 21.8% of the apparent As(III) immobilization (Fig. 5b) (here the physical enmeshment was considered to work within the first 0.5 h because of the significant generation of the flocs). Also, the results indicate that the resulting flocs could create a great number of active binding sites for As species, resulting in about 78.2% of the apparent As(III) immobilization. For the active binding sites, the most likely candidate is suggested to be Ca within the flocs. This is because Ca possesses a higher affinity for As than other components including OFGs in rDBC, particularly under highly alkaline conditions. Based on all the results and analyses, we thus assert that *in-situ* creation of the highly enriched Ca in the nascent flocs predominantly drove the non-oxidative precipitation of As(III), and the oxidative precipitation of As(III) had only slight immobilization effect. Also, the physical enmeshment partially accounted for the apparent As(III) immobilization.

To further confirm our proposed mechanisms, we performed SEM-EDS analysis on the flocs samples (hereafter denoted as rDBC-0.5, rDBC-8, and rDBC-24, respectively) collected from the rDBC/Ca^{2+}/As(III) system at different stages as well as rDBC. As shown in Fig. 6a–6e, rDBC had a relatively smooth surface and predominant contained C and O elements and a slight amount of Ca, but no As. Whilst there was a slight amount of Ca in rDBC, it failed to immobilize the apparent As(III) (Fig. 5a), because the Ca concentration is far too low. In contrast, rDBC-0.5 had fine the stacked particle-like flocs with a rougher surface, which differed significantly from the pristine rDBC sample (Fig. 6f). Furthermore, the corresponding EDS elemental mapping analysis elucidated that, at the micron scale, the element Ca was highly enriched in the flocs, and its elemental distribution was intimately correlated with the elemental distribution of As (Fig. 6i and 6j). However, there was an insignificant correlation between the elemental distributions of C and As as well as Ca. These results suggest that rDBC could greatly facilitate the enrichment of Ca, and the resulting Ca was capable of precipitating As. The C-containing components like aromatic structure in rDBC were not directly associated with the apparent As(III) immobilization, which was confirmed by no apparent As(III) immobilization by rDBC (Fig. 5a). Even after a prolonged reaction time, we still observed almost the same phenomena on the rDBC-8 and rDBC-24 samples (Fig. 6k–6t). The negligible changes in morphologies and chemical compositions of the flocs indicated nearly complete precipitation of Ca with As at the initial stage (corresponding to 0–0.5 h), and it was relatively independent of the reaction time ranging from 0.5 to 24 h.

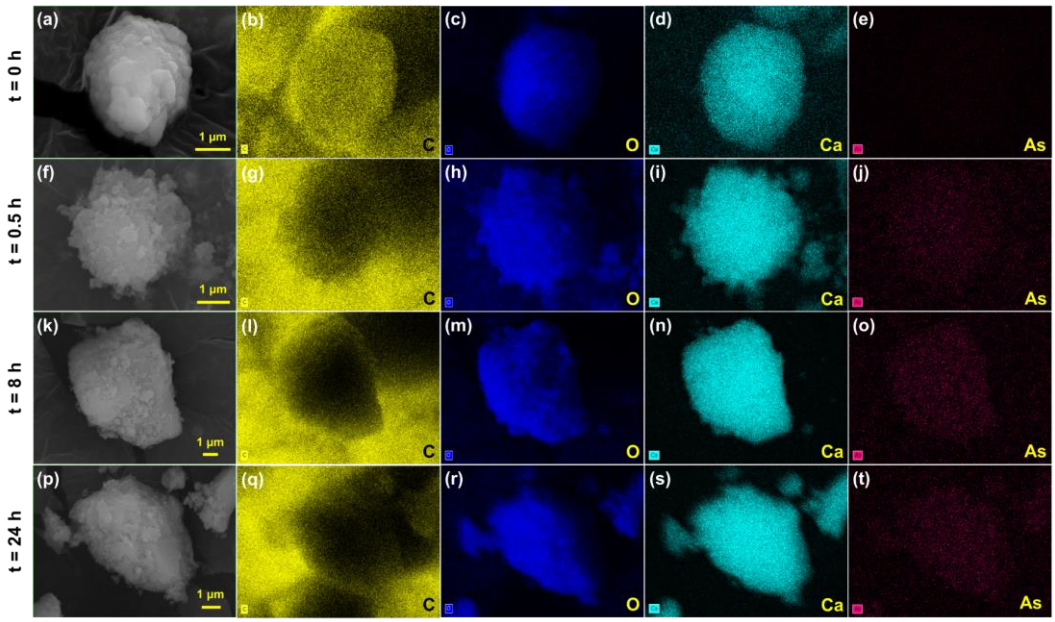

Fig. 6. SEM images (a, f, k, and p) and the corresponding EDS elemental mappings of the freeze-dried samples collected from the rDBC/Ca^{2+}/As(III) system during the As(III) immobilization: element C (b, g, l, and q), O (c, h, m, and r), Ca (d, i, n, and s), As (e, j, o, and t).

FTIR analysis was employed to identify the apparent As(III) immobilization interactions. In contrast to rUBC, rDBC possessed more OFGs including –OH, COOH and C=O, and C–O–C and C–OH, as evidenced by the stronger intensities of characteristic peaks at 3400–3500, 1500–1700, and 1000–1300 cm^{-1}, respectively (Fig. S3a), and this is similar to previous findings (Qu et al., 2016). Furthermore, this was supported by a higher ratio of O/C in rDBC than that in rUBC (Table S1). After the reaction, the characteristic peaks at 1000–1700 cm^{-1} (mainly corresponding to OFGs) underwent either peak shift (i.e., from 1656 to 1644 cm^{-1} and from 1106 to 1039 cm^{-1})

474 or new peak were created at 1410–1490 cm^{-1}. The FTIR spectral changes indicate that
475 OFGs interplayed with Ca^{2+} rather than As likely via complexation and/or Ca^{2+}-
476 bridging modes (Xu et al., 2017), since they possess a higher affinity for Ca^{2+} than As
477 under highly alkaline conditions. In addition, the new peak at 871 cm^{-1} was smaller
478 than that (875 cm^{-1}) of Ca–O–As^{V} and Ca–O, which could be assigned to Ca–O–As^{III}
479 and Ca–O. Other new characteristic peaks occurred at 568–604 cm^{-1}, which were
480 attributed to Ca–O(H) (Myneni, 1998). This suggests the formation of Ca-As(III)
481 precipitates as well as Ca-containing components like $Ca(OH)_2$. After the 0.5 h of
482 reaction time, the relative intensities of these characteristic peaks remained stable,
483 indicating the almost complete formation of Ca-As(III) precipitates as well as Ca-
484 containing components at the initial stage.

485 The As $3d_{5/2}$ XPS spectra analysis revealed that As(III) mainly prevailed in the
486 resulting Ca-As precipitates and agreed with the observed fraction of As species (Fig.
487 7b). A comparison of Ca $2p_{3/2}$ XPS spectra was performed to identify interactions of Ca
488 with As species. For the selected rDBC samples (i.e., rDBC-0.5, rDBC-8, and rDBC-
489 24), the peaks of Ca $2p_{3/2}$ XPS spectra were located at ~347.2 eV, 0.4 eV lower than
490 that (~347.6 eV) of the corresponding rUBC samples (i.e., rUBC-0.5, rUBC-8, and
491 rUBC-24) (Fig. S9). This difference was close to that (0.5 eV) of As $3d_{5/2}$ XPS spectra
492 (~43.7 eV for the rDBC samples vs. ~44.2 eV for the rUBC samples). This implies that
493 the interactions of the enriched Ca with As should be assigned to chemical precipitation,
494 which is analogous to those in the rUBC/Ca^{2+}/As(III) system. The resulting Ca-As(III/V)
495 precipitates (predominant Ca-As(III) precipitates) were identified to be amorphous

minerals, as confirmed by the absence of characteristic XRD patterns (Fig. 7c), which was presumably due to the presence of rDBC and/or the short ageing time. In summary, all the characterizations and analyses have confirmed the proposed As(III) immobilization mechanisms.

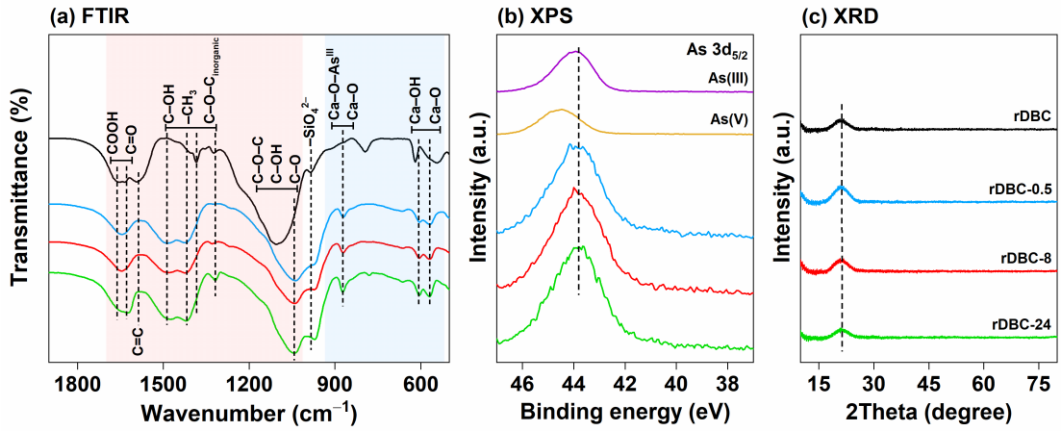

Fig. 7. (a) FTIR spectra, (b) As $3d_{5/2}$ XPS spectra, (c) XRD patterns of the selected rDBC samples.

3.4. Effect of water chemistry on apparent As(III) immobilization

3.4.1. Effect of Ca^{2+} concentration

Ca^{2+} is essential to the apparent As(III) immobilization by both rUBC and rDBC, consequently, we further investigated the effect of Ca^{2+} concentration on the immobilization (0–100 mM). Notably, in the rUBC/Ca^{2+}/As(III) system, the apparent As(III) immobilization increased from 4.8 to 18.7, to 73.1, and to 74.4 μM within 24 h when Ca^{2+} concentration rose from 0 to 10, to 50, and to 100 mM, respectively (Fig. 8a). This was because a higher concentration of Ca^{2+} was able to precipitate a larger amount of the newly generated As(V) from As(III) oxidation by rUBC into the solid

514 phase (Fig. 8b), as confirmed by our prediction results (Fig. 1b). Moreover, the increase
515 in apparent As(III) immobilization rate could be seen with the increasing Ca^{2+}
516 concentration. The increase in Ca^{2+} concentration could substantially neutralize the
517 negative surface charge of rUBC (Fig. S2), thus facilitating As(V) generation by
518 weakening the electrostatic repulsion between rUBC and As(III) anions (Fig. 8b). This
519 could increase the precipitation of subsequent As(V) with Ca^{2+}. These results indicate
520 that the increase in Ca^{2+} concentration favored the As(III) oxidative immobilization.

521 Similarly, we observed that increasing Ca^{2+} concentration significantly promoted
522 the apparent As(III) immobilization in the rDBC/Ca^{2+}/As(III) system (Fig. 8c).
523 However, we found that further increasing Ca^{2+} concentration impeded the As(III)
524 oxidation by rDBC, as verified by a lower As(V) concentration (Fig. 8d). This was
525 because a higher Ca concentration within the flocs exerted a stronger inhibition for
526 electron transfers between As(III) and rDBC. Considering our previous FTIR analysis
527 (Fig. 7a), this inhibition further revealed that the Ca-As(III) precipitates occurred within
528 the flocs via a ternary rDBC-Ca-As(III) complex by Ca^{2+}-bridging interactions between
529 As(III) and the OFGs of rDBC. Furthermore, a higher apparent As(III) immobilization
530 but a lower As(V) generation concentration suggested that elevating Ca^{2+} concentration
531 enhanced the apparent As(III) immobilization via direct precipitation of As(III) with
532 Ca^{2+}. It is worth noting that for both the ternary systems, increasing Ca^{2+} concentration
533 beyond 50 mM has a negligible effect on the apparent As(III) immobilization (Fig. 8a
534 and 8c). This might be due to that available amounts of the active binding sites for As
535 species have reached saturation when Ca^{2+} concentration was increased to about 50 mM

in the presence of rUBC and rDBC.

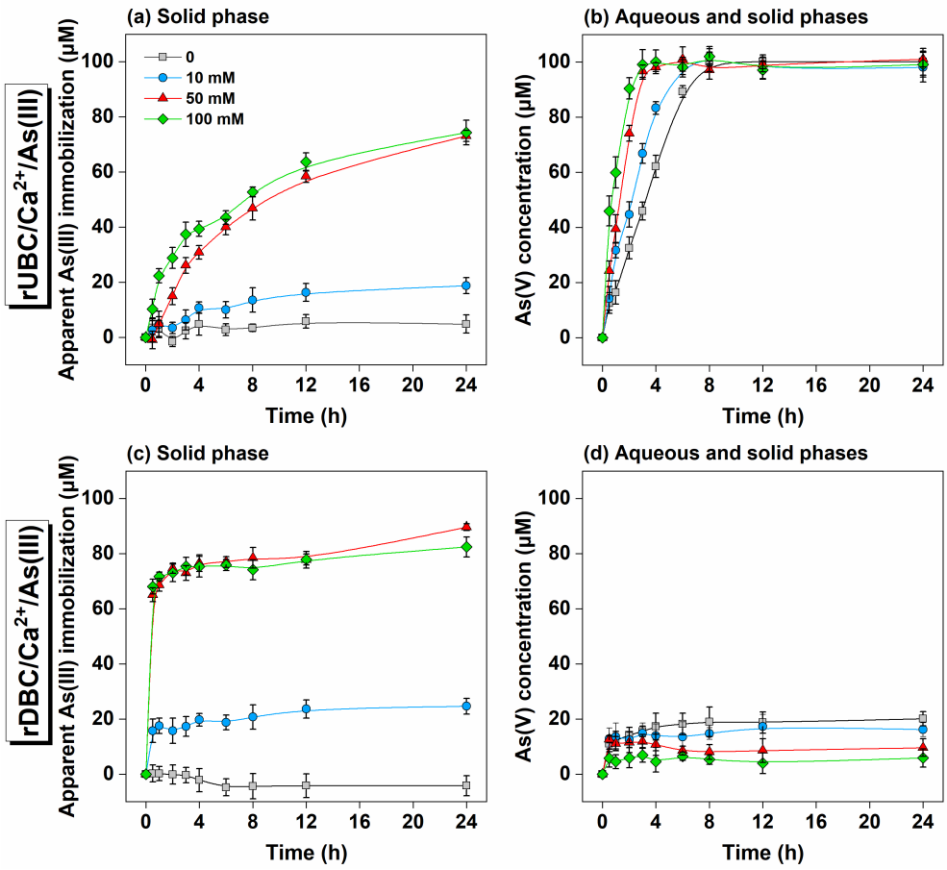

Fig. 8. Effect of Ca^{2+} concentration on apparent As(III) immobilization (a and c) and As(V) generation (b and d) in the rUBC/Ca^{2+}/As(III) and rDBC/Ca^{2+}/As(III) systems.

3.4.2. Effect of solution pH

Similar to Ca^{2+}, increasing solution pH favored the apparent As(III) immobilization. In the rUBC/Ca^{2+}/As(III) system, the apparent As(III) immobilization increased significantly from 29.9 to 73.1, and to 89.9 μM with the pH increasing from 10.0 to 11.5, and to 12.5, respectively (Fig. 9a). This could be explained by increased chemical precipitation of As(V) with Ca^{2+} and/or adsorption of As(V) onto the newly generated $Ca(OH)_2$ at a higher pH value (Figs. 1b and S5). Also, we observed the

549 accelerated apparent As(III) immobilization rate with the increasing solution pH. This
550 was because the increase in As(V) generation rate facilitated subsequent As(V)
551 precipitation with Ca^{2+} at a higher pH value (Fig. 9a and 9b). With respect to the
552 accelerated oxidation of As(III) to As(V) by rUBC, it might be due to a larger redox
553 potential gap between redox couples on rUBC and As(V)/As(III) couples at a higher
554 pH value (Zhong et al., 2019). These results indicate that elevating solution pH could
555 stimulate As(III) oxidation and subsequent precipitation of As(V) with Ca^{2+}, further
556 corroborating the proposed As(III) oxidative immobilization. In the rDBC/Ca^{2+}/As(III)
557 systems, the apparent As(III) immobilization increased markedly from 30.3 to 89.6, and
558 then to 100 μM, respectively, as solution pH elevated from 10.0 to 11.5, and then to
559 12.5 (Fig. 9c). These observations indicate that a higher solution pH encouraged the
560 apparent As(III) immobilization. A possible explanation involved a greater extent of
561 chemical precipitation of As with Ca^{2+} and/or adsorption of As species onto solid
562 $Ca(OH)_2$ at a higher solution pH (Figs. 1b and S5). Meantime, the newly generated
563 As(V) concentration increased from 8.3 to 9.6, and to 22.7 μM, respectively (Fig. 9d),
564 indicating that the increasing solution pH improved the As(III) oxidation extent. The
565 enhanced oxidation of As(III) to As(V) was possibly attributed to the increasing redox
566 potential gap between redox couples on rDBC and As(V)/As(III) couples with the
567 elevating solution pH, which is similar to the Eh-pH diagrams for reduced NOM-As
568 system (Jiang et al., 2009). In conclusion, the increase in the solution pH promoted the
569 apparent As(III) immobilization in both the rUBC/Ca^{2+}/As(III) and the
570 rDBC/Ca^{2+}/As(III) systems.

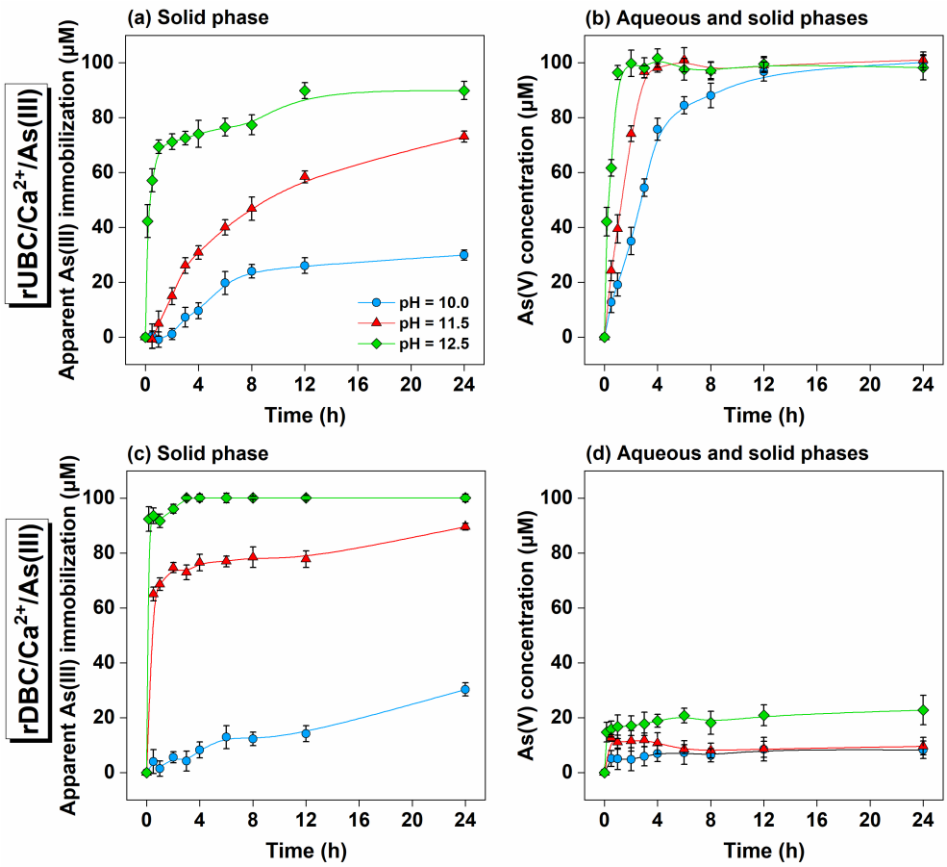

571

572 **Fig. 9.** Effect of solution pH on apparent As(III) immobilization (a and c) and As(V)

573 generation (b and d) in the rUBC/Ca^{2+}/As(III) and rDBC/Ca^{2+}/As(III) systems.

574

575 *3.5. Environmental significance*

576 High-As groundwater is widely distributed worldwide (e.g., calcareous regions)

577 and poses a great threat to public health. The geochemical processes determining the

578 fate of As are often affected by both natural and engineered components. Our work

579 describes the positive effects of the undissolved and dissolved fractions of reduced

580 biochar on the abiotic oxidation and immobilization of As(III) in simulated anoxic

581 groundwater of calcareous regions, largely relieving the As environmental risk. Our

582 investigation further confirms that both rUBC and rDBC can remove 72.4% and 72.1%

583 of As(tot) from real groundwater (collected from a local village in Hunan province)

584 spiked with 100 μM As(III), respectively (Table S2). To the best of our knowledge, the
585 large (r)UBC particles often have difficulty in entering into subsurface environments,
586 thus only a small amount of rUBC may be present in natural subsurface environments.
587 Furthermore, rUBC has a lower As(III) immobilization capacity than rDBC in anoxic
588 Ca^{2+}-rich groundwater (Fig. S10). Consequently, rUBC may have a lower impact on
589 the oxidation and immobilization of As(III) in natural subsurface environments,
590 particularly under long-term and strongly reducing conditions. In contrast, a massive
591 amount of rDBC can be readily introduced into the subsurface environment and govern
592 the apparent As(III) immobilization via the non-oxidative As(III) precipitation. As a
593 consequence, rDBC may deserve more attention on the fate of As(III) in typical
594 calcareous regions. We acknowledge that natural subsurface environment is more
595 complicated than the currently studied systems, and thus further investigations (e.g.,
596 effect of co-existing anions including phosphate and carbonate) need to be examined to
597 advance our understanding of engineered black carbon such as biochar on the fate of
598 As(III) in the subsurface environment close to real calcareous aquifers.
599

600 ## 4. Conclusions

601 This study reports that As(III) in anoxic Ca^{2+}-rich groundwater can be efficiently
602 immobilized by both the undissolved and dissolved fractions of reduced biochar via
603 contrasting interaction mechanisms under alkaline conditions. Our results reveal that
604 rUBC completely oxidized As(III) to As(V) and subsequently precipitated with Ca^{2+}
605 adsorbed/precipitated on its surface. In contrast, rDBC underwent a flocculation

process induced by Ca^{2+}, thus forming the extremely enriched-Ca^{2+} in the flocs that predominantly drives precipitation with As(III). Meanwhile, both physical enmeshment of As(III) by the nascent flocs and As(III) oxidative precipitation slightly account for the apparent As(III) immobilization. The apparent As(III) immobilization depends strongly on water chemistry, including Ca^{2+} concentration and solution pH. Both the increases in Ca^{2+} concentration and solution pH can significantly promote the apparent As(III) immobilization. Our findings elucidate the unintended environmental effects of undissolved and dissolved fractions of biochar on the fate of As(III) in aquifers of calcareous regions. This study may suggest an alternative strategy candidate for remediation of high-As groundwater of calcareous regions by injecting (nano)biochar suspension.

Acknowledgments

This work was supported by the National Natural Science Foundation of China (No. 41671311), National Key Research and Development Program of China (No. 2019YFC1805202), State Key Laboratory of Pollution Control and Resource Reuse Foundation (No. PCRRF18027), and Program for HUST Academic Frontier Youth Team (No. 2018QYTD05). The authors would like to thank the Analytical and Testing Center, Huazhong University of Science and Technology, China, for the help on sample characterization and Xuelin Dong and Dan Zhu in Hubei Geological Research Laboratory for the assistance in SEM-EDS characterization. The authors also appreciate the support from the Brook Byers Institute for Sustainable Systems, Hightower Chair

and Georgia Research Alliance at the Georgia Institute of Technology. The views and ideas expressed herein are solely those of the authors and do not represent the ideas of the funding agencies in any form.

References

Barnes, I., Presser, T.S., Saines, M., Dickson, P., Van Groos, A.F.K., 1982. Geochemistry of highly basic calcium hydroxide groundwater in Jordan. Chem. Geol. 35, 147–154.

Beiyuan, J., Awad, Y.M., Beckers, F., Tsang, D.C.W., Ok, Y.S., Rinklebe, J., 2017. Mobility and phytoavailability of As and Pb in a contaminated soil using pine sawdust biochar under systematic change of redox conditions. Chemosphere 178, 110–118.

Bortone, I., Di Nardo, A., Di Natale, M., Erto, A., Musmarra, D., Santonastaso, G.F., 2013. Remediation of an aquifer polluted with dissolved tetrachloroethylene by an array of wells filled with activated carbon. J. Hazard. Mater. 260, 914–920.

Cao, X., Ma, L., Liang, Y., Gao, B., Harris, W., 2011. Simultaneous immobilization of lead and atrazine in contaminated soils using dairy-manure biochar. Environ. Sci. Technol. 45, 4884–4889.

Costagliola, P., Bardelli, F., Benvenuti, M., Di Benedetto, F., Lattanzi, P., Romanelli, M., Paolieri, M., Rimondi, V., Vaggelli, G., 2013. Arsenic-bearing calcite in natural travertines: Evidence from sequential extraction, μXAS, and μXRF. Environ. Sci. Technol. 47, 6231–6238.

Dong, X., Ma, L.Q., Gress, J., Harris, W., Li, Y., 2014. Enhanced Cr(VI) reduction and As(III) oxidation in ice phase: Important role of dissolved organic matter from biochar. J. Hazard. Mater. 267, 62–70.

Fendorf, S., Michael, H.A., van Geen, A., 2010. Spatial and temporal variations of groundwater arsenic in South and Southeast Asia. Science 328, 1123.

Goh, K.-H., Lim, T.-T., 2004. Geochemistry of inorganic arsenic and selenium in a

656 tropical soil: effect of reaction time, pH, and competitive anions on arsenic and
657 selenium adsorption. Chemosphere 55, 849–859.
658 Guo, H., Wen, D., Liu, Z., Jia, Y., Guo, Q., 2014. A review of high arsenic groundwater
659 in mainland and Taiwan, China: Distribution, characteristics and geochemical
660 processes. Appl. Geochem. 41, 196–217.
661 He, R., Peng, Z., Lyu, H., Huang, H., Nan, Q., Tang, J., 2018. Synthesis and
662 characterization of an iron-impregnated biochar for aqueous arsenic removal. Sci.
663 Total Environ. 612, 1177–1186.
664 Hu, C.-Y., Lo, S.-L., Kuan, W.-H., 2014. High concentration of arsenate removal by
665 electrocoagulation with calcium. Sep. Purif. Technol. 126, 7–14.
666 Jiang, C., Garg, S., Waite, T.D., 2017. Iron redox transformations in the presence of
667 natural organic matter: Effect of calcium. Environ. Sci. Technol. 51, 10413–10422.
668 Jiang, J., Bauer, I., Paul, A., Kappler, A., 2009. Arsenic redox changes by microbially
669 and chemically formed semiquinone radicals and hydroquinones in a humic
670 substance model quinone. Environ. Sci. Technol. 43, 3639–3645.
671 Jin, J., Sun, K., Wang, Z., Yang, Y., Han, L., Xing, B., 2017. Characterization and
672 phenanthrene sorption of natural and pyrogenic organic matter fractions. Environ.
673 Sci. Technol. 51, 2635–2642.
674 Karim, M.M., 2000. Arsenic in groundwater and health problems in Bangladesh. Water
675 Res. 34, 304–310.
676 Lawson, M., Polya, D.A., Boyce, A.J., Bryant, C., Mondal, D., Shantz, A., Ballentine,
677 C.J., 2013. Pond-derived organic carbon driving changes in arsenic hazard found
678 in Asian groundwaters. Environ. Sci. Technol. 47, 7085–7094.
679 Lian, F., Xing, B., 2017. Black carbon (biochar) In water/soil environments: Molecular
680 structure, sorption, stability, and potential risk. Environ. Sci. Technol. 51,
681 13517−13532.
682 Liu, T., Tsang, D.C.W., Lo, I.M.C., 2008. Chromium(VI) reduction kinetics by zero-
683 valent iron in moderately hard water with humic acid: Iron dissolution and humic
684 acid adsorption. Environ. Sci. Technol. 42, 2092–2098.

685 Mackenzie, K., Bleyl, S., Georgi, A., Kopinke, F.-D., 2012. Carbon-iron–An Fe/AC
686 composite–As alternative to nano-iron for groundwater treatment. Water Res. 46,
687 3817–3826.
688 Mak, M.S.H., Rao, P., Lo, I.M.C., 2009. Effects of hardness and alkalinity on the
689 removal of arsenic(V) from humic acid-deficient and humic acid-rich groundwater
690 by zero-valent iron. Water Res. 43, 4296–4304.
691 Mariner, P.E., Holzmer, F.J., Jackson, R.E., Meinardus, H.W., Wolf, F.G., 1996. Effects
692 of high pH on arsenic mobility in a shallow sandy aquifer and on aquifer
693 permeability along the adjacent shoreline, commencement bay superfund site,
694 Tacoma, Washington. Environ. Sci. Technol. 30, 1645–1651.
695 Marshall, J.A., Morton, B.J., Muhlack, R., Chittleborough, D., Kwong, C.W., 2017.
696 Recovery of phosphate from calcium-containing aqueous solution resulting from
697 biochar-induced calcium phosphate precipitation. J. Clean. Prod. 165, 27–35.
698 Martínez-Villegas, N., Briones-Gallardo, R., Ramos-Leal, J.A., Avalos-Borja, M.,
699 Castañón-Sandoval, A.D., Razo-Flores, E., Villalobos, M., 2013. Arsenic mobility
700 controlled by solid calcium arsenates: A case study in Mexico showcasing a
701 potentially widespread environmental problem. Environ. Pollut. 176, 114–122.
702 Michael, H.A., 2013. An arsenic forecast for China. Science 341, 852.
703 Myneni, S., 1998. Arsenate interactions with CaO: Formation of johnbaumite. Mineral.
704 Mag. 62, 1050–1051.
705 Niazi, N.K., Bibi, I., Shahid, M., Ok, Y.S., Burton, E.D., Wang, H., Shaheen, S.M.,
706 Rinklebe, J., Lüttge, A., 2018a. Arsenic removal by Perilla leaf biochar in aqueous
707 solutions and groundwater: An integrated spectroscopic and microscopic
708 examination. Environ. Pollut. 232, 31–41.
709 Niazi, N.K., Bibi, I., Shahid, M., Ok, Y.S., Shaheen, S.M., Rinklebe, J., Wang, H.,
710 Murtaza, B., Islam, E., Farrakh Nawaz, M., Lüttge, A., 2018b. Arsenic removal by
711 Japanese Oak wood biochar in aqueous solutions and well water: Investigating
712 arsenic fate using integrated spectroscopic and microscopic techniques. Sci. Total
713 Environ. 621, 1642–1651.

714 Palmer, N.E., von Wandruszka, R., 2001. Dynamic light scattering measurements of
715 particle size development in aqueous humic materials. Fresenius' J. Anal. Chem.
716 371, 951–954.
717 Podgorski, J.E., Eqani, S.A.M.A.S., Khanam, T., Ullah, R., Shen, H., Berg, M., 2017.
718 Extensive arsenic contamination in high-pH unconfined aquifers in the Indus
719 Valley. Sci. Adv. 3, e1700935.
720 Qian, A., Yuan, S., Zhang, P., Tong, M., 2015. A new mechanism in electrochemical
721 process for arsenic oxidation: Production of H2O2 from Anodic O2 reduction on
722 the cathode under automatically developed alkaline conditions. Environ. Sci.
723 Technol. 49, 5689–5696.
724 Qiao, J.-t., Li, X.-m., Hu, M., Li, F.-b., Young, L.Y., Sun, W.-m., Huang, W., Cui, J.-h.,
725 2018. Transcriptional activity of arsenic-reducing bacteria and genes regulated by
726 lactate and biochar during arsenic transformation in flooded paddy soil. Environ.
727 Sci. Technol. 52, 61–70.
728 Qin, W., Wang, Y., Fang, G., Wu, T., Liu, C., Zhou, D., 2016. Evidence for the
729 generation of reactive oxygen species from hydroquinone and benzoquinone:
730 Roles in arsenite oxidation. Chemosphere 150, 71−78.
731 Qu, X., Fu, H., Mao, J., Ran, Y., Zhang, D., Zhu, D., 2016. Chemical and structural
732 properties of dissolved black carbon released from biochars. Carbon 96, 759–767.
733 Rauch-Williams, T., Hoppe-Jones, C., Drewes, J.E., 2010. The role of organic matter in
734 the removal of emerging trace organic chemicals during managed aquifer recharge.
735 Water Res. 44, 449–460.
736 Reza, A.H.M.S., Jean, J.-S., Lee, M.-K., Liu, C.-C., Bundschuh, J., Yang, H.-J., Lee, J.-
737 F., Lee, Y.-C., 2010. Implications of organic matter on arsenic mobilization into
738 groundwater: Evidence from northwestern (Chapai-Nawabganj), central
739 (Manikganj) and southeastern (Chandpur) Bangladesh. Water Res. 44, 5556–5574.
740 Roden, E.E., Kappler, A., Bauer, I., Jiang, J., Paul, A., Stoesser, R., Konishi, H., Xu, H.,
741 2010. Extracellular electron transfer through microbial reduction of solid-phase
742 humic substances. Nat. Geosci. 3, 417–421.

743 Rodríguez-Lado, L., Sun, G., Berg, M., Zhang, Q., Xue, H., Zheng, Q., Johnson, C.A.,
744 2013. Groundwater arsenic contamination throughout China. Science 341, 866.
745 Sadergaski, L.R., Said, M., Hixon, A.E., 2019. Calcium-facilitated aggregation and
746 precipitation of the uranyl peroxide nanocluster U60 in the presence of Na-
747 montmorillonite. Environ. Sci. Technol. 53, 4922–4930.
748 Scott, D.T., McKnight, D.M., Blunt-Harris, E.L., Kolesar, S.E., Lovley, D.R., 1998.
749 Quinone moieties act as electron acceptors in the reduction of humic substances by
750 humics-reducing microorganisms. Environ. Sci. Technol. 32, 2984–2989.
751 Smedley, P.L., Kinniburgh, D.G., 2002. A review of the source, behaviour and
752 distribution of arsenic in natural waters. Appl. Geochem. 17, 517–568.
753 Tokunaga, S., 1999. Removal of arsenic(III) and arsenic(V) Ions from aqueous
754 solutions with lanthanum(III) salt and comparison with aluminum(III), calcium(II),
755 and iron(III) salts. Water Environ. Res. 71, 299–306.
756 Van Vinh, N., Zafar, M., Behera, S.K., Park, H.S., 2015. Arsenic(III) removal from
757 aqueous solution by raw and zinc-loaded pine cone biochar: equilibrium, kinetics,
758 and thermodynamics studies. Int. J. Environ. Sci. Technol. 12, 1283–1294.
759 Vithanage, M., Herath, I., Joseph, S., Bundschuh, J., Bolan, N., Ok, Y.S., Kirkham,
760 M.B., Rinklebe, J., 2017. Interaction of arsenic with biochar in soil and water: A
761 critical review. Carbon 113, 219–230.
762 Wan, Z., Sun, Y., Tsang, D.C.W., Hou, D., Cao, X., Zhang, S., Gao, B., Ok, Y.S., 2020.
763 Sustainable remediation with an electroactive biochar system: Mechanisms and
764 perspectives. Green Chem. 22, 2688–2711.
765 Wang, L., Chen, L., Tsang, D.C.W., Zhou, Y., Rinklebe, J., Song, H., Kwon, E.E., Baek,
766 K., Sik Ok, Y., 2019. Mechanistic insights into red mud, blast furnace slag, or
767 metakaolin-assisted stabilization/solidification of arsenic-contaminated sediment.
768 Environ. Int. 133, 105247.
769 Wei, A., Ma, J., Chen, J., Zhang, Y., Song, J., Yu, X., 2018. Enhanced nitrate removal
770 and high selectivity towards dinitrogen for groundwater remediation using biochar-
771 supported nano zero-valent iron. Chem. Eng. J. 353, 595–605.

772 Winkel, L.H.E., Casentini, B., Bardelli, F., Voegelin, A., Nikolaidis, N.P., Charlet, L.,
773 2013. Speciation of arsenic in Greek travertines: Co-precipitation of arsenate with
774 calcite. Geochim. Cosmochim. Acta 106, 99–110.
775 Wongrod, S., Simon, S., van Hullebusch, E.D., Lens, P.N.L., Guibaud, G., 2019.
776 Assessing arsenic redox state evolution in solution and solid phase during As(III)
777 sorption onto chemically-treated sewage sludge digestate biochars. Bioresource
778 Technol. 275, 232–238.
779 Xu, F., Wei, C., Zeng, Q., Li, X., Alvarez, P.J.J., Li, Q., Qu, X., Zhu, D., 2017.
780 Aggregation behavior of dissolved black carbon: Implications for vertical mass
781 flux and fractionation in aquatic systems. Environ. Sci. Technol. 51, 13723–13732.
782 Yang, F., Xu, Z., Yu, L., Gao, B., Xu, X., Zhao, L., Cao, X., 2018a. Kaolinite enhances
783 the stability of the dissolvable and undissolvable fractions of biochar via different
784 mechanisms. Environ. Sci. Technol. 52, 8321–8329.
785 Yang, X., Igalavithana, A.D., Oh, S.-E., Nam, H., Zhang, M., Wang, C.-H., Kwon, E.E.,
786 Tsang, D.C.W., Ok, Y.S., 2018b. Characterization of bioenergy biochar and its
787 utilization for metal/metalloid immobilization in contaminated soil. Sci. Total
788 Environ. 640–641, 704-713.
789 Yang, X., Tsibart, A., Nam, H., Hur, J., El-Naggar, A., Tack, F.M.G., Wang, C.-H., Lee,
790 Y.H., Tsang, D.C.W., Ok, Y.S., 2019. Effect of gasification biochar application on
791 soil quality: Trace metal behavior, microbial community, and soil dissolved organic
792 matter. J. Hazard. Mater. 365, 684–694.
793 Yao, Y., Gao, B., Chen, J., Yang, L., 2013. Engineered biochar reclaiming phosphate
794 from aqueous solutions: Mechanisms and potential application as a slow-release
795 fertilizer. Environ. Sci. Technol. 47, 8700–8708.
796 Yates, L.M., von Wandruszka, R., 1999. Effects of pH and metals on the surface tension
797 of aqueous humic materials. Soil Sci. Soc. Am. J. 63, 1645–1649.
798 Zhang, D., Yuan, Z., Wang, S., Jia, Y., Demopoulos, G.P., 2015. Incorporation of arsenic
799 into gypsum: Relevant to arsenic removal and immobilization process in
800 hydrometallurgical industry. J. Hazard. Mater. 300, 272–280.

Zhang, L., Yang, H., 2013. Transport process of arsenic in karst subterranean stream and analysis on the influence factors: a case in Lihu subterranean stream of Nandan county, Guangxi. Carsologica Sin. 32, 377–383.

Zhong, D., Jiang, Y., Zhao, Z., Wang, L., Chen, J., Ren, S., Liu, Z., Zhang, Y., Tsang, D.C.W., Crittenden, J.C., 2019. pH dependence of arsenic oxidation by rice-husk-derived biochar: Roles of redox-active moieties. Environ. Sci. Technol. 53, 9034–9044.

Zhong, D., Zhang, Y., Wang, L., Chen, J., Jiang, Y., Tsang, D.C.W., Zhao, Z., Ren, S., Liu, Z., Crittenden, J.C., 2018. Mechanistic insights into adsorption and reduction of hexavalent chromium from water using magnetic biochar composite: Key roles of Fe_3O_4 and persistent free radicals. Environ. Pollut. 243, 1302–1309.

Zimmerman, A.R., 2010. Abiotic and microbial oxidation of laboratory-produced black carbon (biochar). Environ. Sci. Technol. 44, 1295–1301.